Resolving Vacuum Fluctuations in an Electrical Circuit by Measuring the Lamb Shift

A. Fragner,[1] M. Göppl,[1] J. M. Fink,[1] M. Baur,[1] R. Bianchetti,[1] P. J. Leek,[1] A. Blais,[2] A. Wallraff[1]*

Quantum theory predicts that empty space is not truly empty. Even in the absence of any particles or radiation, in pure vacuum, virtual particles are constantly created and annihilated. In an electromagnetic field, the presence of virtual photons manifests itself as a small renormalization of the energy of a quantum system, known as the Lamb shift. We present an experimental observation of the Lamb shift in a solid-state system. The strong dispersive coupling of a superconducting electronic circuit acting as a quantum bit (qubit) to the vacuum field in a transmission-line resonator leads to measurable Lamb shifts of up to 1.4% of the qubit transition frequency. The qubit is also observed to couple more strongly to the vacuum field than to a single photon inside the cavity, an effect that is explained by taking into account the limited anharmonicity of the higher excited qubit states.

The concept of the vacuum field was originally invoked as an explanation for the natural linewidths of atoms in free space and given its physical interpretation in terms of virtual particles within the framework of quantum field theory (*1*). The electromagnetic vacuum leads to a number of observable effects (*2*), most notably the Casimir forces (*3*), which cause mechanical displacements of parallel conducting plates in vacuum; the Purcell effect (*4*), which governs the spontaneous emission of a quantum system coupled to a cavity field; and the Lamb shift (*5*, *6*), a radiative level shift that was first observed in hydrogen atoms. The Lamb shift has since been investigated in a number of experiments in the atomic domain (*7*–*9*), in which it is also being established as an ultra-high precision test of the theory of quantum electrodynamics (QED) (*10*). The interaction with the vacuum fluctuations is the underlying reason for the spontaneous emission of radiation from any excited quantum system (*11*). The same effect also triggers the well-known process of vacuum Rabi oscillations in cavity QED (*12*–*15*). Quantum fluctuations have been demonstrated to determine the spontaneous emission lifetime of superconducting quantum bits (qubits) (*16*); they also serve as a benchmark for amplifiers and the squeezing of quantum noise at the quantum limit (*17*, *18*) or for detecting the zero-point motion of nanomechanical oscillators (*19*).

We observed the cavity-enhanced Lamb shift of an individual superconducting two-level system coupled to a high-quality factor resonator with a large vacuum-field strength (*14*) in an architecture known as circuit QED (*20*, *21*). Our measurements were carried out with a superconducting transmon-type qubit (*22*), a Cooper pair box (*23*) with a large ratio of Josephson-to-charging-energy (E_J/E_C). Its energy-level spectrum (*22*) is controlled by a flux Φ threading the loop formed by the two parallel Josephson junctions (Fig. 1B) that determine the Josephson energy $E_J = E_J^{max}|\cos(\pi\Phi/\Phi_0)|$, where E_J^{max} is the maximum Josephson energy of the two tunnel junctions and Φ_0 is the magnetic flux quantum. The electrostatic energy of the qubit $E_C = e^2/2C_\Sigma$ is determined by its total capacitance C_Σ, with e being the electron charge. The qubit is strongly coupled to a coplanar transmission-line resonator (*20*, *21*) with a fundamental resonance frequency $\omega_r/2\pi = 6.44$ GHz and a photon decay rate $\kappa/2\pi \approx 1.6$ MHz. The transmon qubit provides for both a large dipole-coupling strength to the resonator

[1]Department of Physics, Eidgenössische Technische Hochschule–Zurich (ETHZ), CH-8093 Zurich, Switzerland. [2]Département de Physique, Université de Sherbrooke, Sherbrooke, Québec J1K 2R1, Canada.

*To whom correspondence should be addressed. E-mail: andreas.wallraff@phys.ethz.ch.

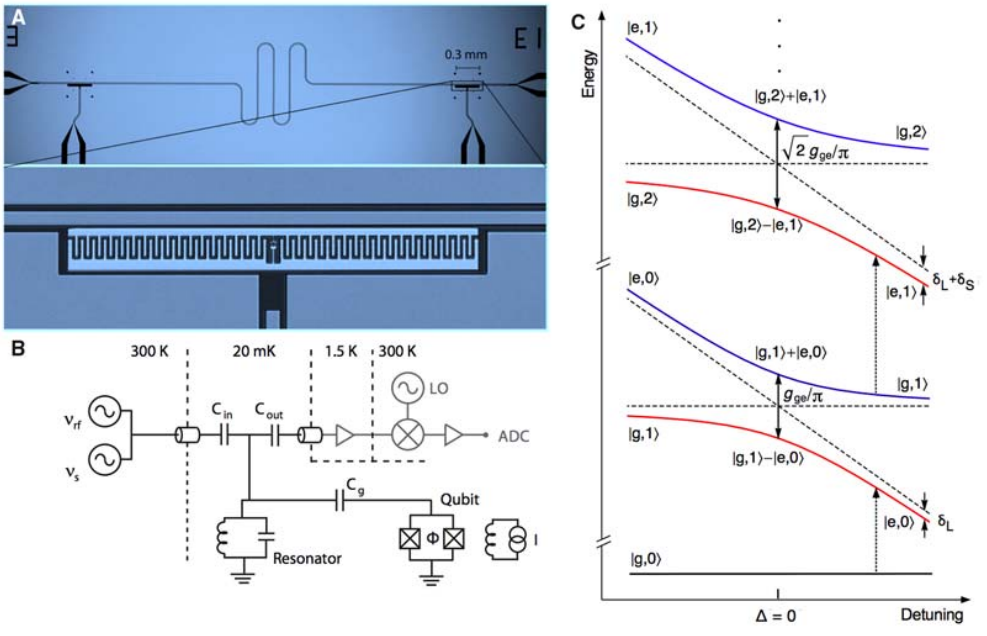

Fig. 1. Sample, experimental setup and energy-level diagram. (**A**) (Top) Optical image of the superconducting coplanar waveguide resonator with the transmon-type superconducting qubit embedded at the position shown boxed. (Bottom) Magnified view of boxed area, showing the qubit with dimensions 300 by 30 μm^2 close to the center conductor. (**B**) Simplified circuit diagram of the setup, similar to the one used in (*21*). We capacitively coupled the qubit at temperature 20 mK to the radiation field contained in the resonator through C_g. We coupled the resonator, represented by a parallel LC circuit, to input and output transmission lines via the capacitors C_{in} and C_{out}. We controlled the qubit transition frequency via a current-biased (I) coil generating a magnetic flux Φ threading the qubit loop. Microwave signal generators for populating the resonator with photons (ν_{rf}) and for exciting the qubit spectroscopically (ν_s) are shown. By using ultralow-noise amplifiers at 1.5 K and a mixer at 300 K, we down-converted the transmitted microwave signal with a local oscillator (LO) and digitized with an analog-to-digital converter (ADC) for measuring the qubit and photon states. (**C**) Energy levels of the coupled (solid lines) and uncoupled (dashed lines) qubit/cavity system versus detuning Δ. The corresponding states and their characteristic energy shifts are indicated (see text for details).

(*14*, *24*) and long relative coherence times at the expense of limited anharmonicity in the energy-level spectrum (*16*, *22*, *25*). Optical images of our device and a simplified circuit diagram of the setup are shown in Fig. 1, A and B.

The coupled qubit/cavity system is well described by a Jaynes-Cummings Hamiltonian

$$\hat{H} = \hbar\omega_{ge}\hat{\sigma}_{ee} + \hbar\omega_r\hat{a}^\dagger\hat{a} + \hbar g_{ge}(\hat{\sigma}_{ge}^\dagger\hat{a} + \hat{a}^\dagger\hat{\sigma}_{ge}) \quad (1)$$

where ω_{ge} denotes the transition frequency from the ground state ($|g\rangle$) to excited state ($|e\rangle$) of the qubit and $\hat{\sigma}_{ij} = |i\rangle\langle j|$ are the corresponding operators acting on the qubit states. The dynamics of the cavity field of frequency ω_r is described by the creation and annihilation operators $\hat{a}^\dagger$, $\hat{a}$ acting on the photon number states $|n\rangle$ and the dipole coupling strength between qubit and cavity is given by g_{ge}. Equation 1 can be generalized to take into account additional qubit levels (*22*, *24*).

In the resonant limit $\Delta = \omega_{ge} - \omega_r \to 0$, a single quantum of energy is coherently exchanged between the qubit and the cavity (*21*, *24*), which are described by the joint-dressed qubit-field state vectors $|n\pm\rangle \equiv (|g,n\rangle \pm |e,n-1\rangle)/\sqrt{2}$ (Fig. 1C). A qualitatively different regime is obtained when qubit and cavity are far detuned from each other ($|\Delta| >> g_{ge}$). In this dispersive limit, the two systems do not exchange energy resonantly, instead their interaction manifests itself in the form of frequency shifts (*20*, *21*, *26*). The qubit transition frequency ω_{ge} is renormalized by the dispersive interaction and experiences a detuning-dependent ac Stark shift $\delta_S \sim 2\, n\, g_{ge}^2/\Delta$ for a cavity field populated with $n = \langle\hat{a}^\dagger\hat{a}\rangle$ photons (*26*), as well as a Lamb shift $\delta_L \sim g_{ge}^2/\Delta$ due to its interaction with the vacuum fluctuations, $\langle\hat{a}^\dagger\hat{a}\rangle = 0$ (Fig. 1C). In our circuit QED setup, we are able to adjust the size of the Lamb and Stark shifts by controlling the detuning Δ between the resonator frequency and the qubit frequency. A similar approach has been used in an experiment with Rydberg atoms interacting with the vacuum field in a three-dimensional microwave cavity (*8*).

To resolve the relatively small Lamb shift of our solid-state quantum system, an accurate measurement of the characteristic qubit parameters and their dependence on the control variables was essential. We determined the qubit transition frequency and its periodic modulation with applied magnetic flux by measuring the cavity-transmission spectrum (*24*) and simultaneously performing qubit spectroscopy with a dispersive measurement of the cavity frequency shift (*26*). With this procedure, we can determine both the flux periodicity and the flux offset because of magnetic offset fields to an accuracy of better than $10^{-3}\,\Phi_0$. From here on, we express the applied magnetic field in terms of a normalized flux Φ/Φ_0. Adjusting the applied flux bias to $\Phi/\Phi_0 = 0$, the qubit is tuned to its maximum transition frequency $\omega_{ge}/2\pi = 7.84$ GHz, which we determined spectroscopically. At this bias point, we also determined the transition frequency $\omega_{gf}/2\pi$ between ground $|g\rangle$ and second excited qubit state $|f\rangle$ via two-photon absorption spectroscopy (*22*, *25*), which yields an anharmonicity of $\alpha = (\omega_{ge} - \omega_{ef})/2\pi \sim 250$ MHz. With these two quantities, we were able to in turn determine the maximum Josephson coupling energy $E_J^{max} = 35.11$ GHz and the charging energy of our device $E_C = 231.7$ MHz at maximum positive detuning from the cavity, in which the dispersive shifts are small. To check for consistency, similar measurements have been performed down to negative detunings of $|\Delta|/2\pi \sim 3$ GHz. The excitation spectrum of our qubit, including its higher excited states, is fully determined by E_J^{max}, E_C, and the flux periodicity (*22*).

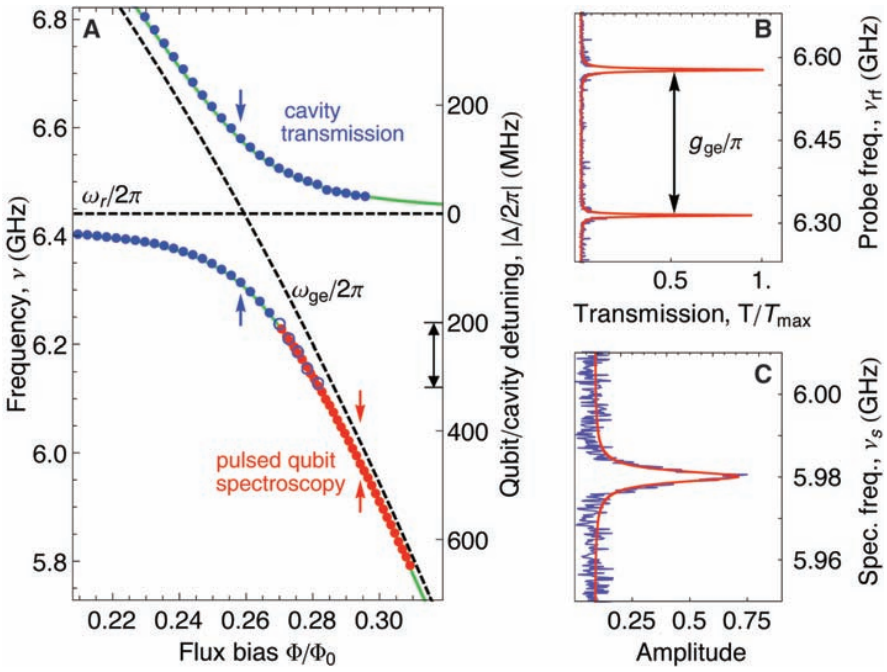

Fig. 2. Spectrum of the coupled qubit/cavity system. (**A**) Measured transition frequencies of cavity (blue circles) and qubit (red circles) versus normalized flux bias Φ/Φ_0. The dashed horizontal line is the cavity transition frequency ω_r, and the dashed slanted line is the calculated bare qubit-transtion frequency ω_{ge}. The green solid lines are the numerically calculated eigenfrequencies of the coupled system. Overlap of resonator transmission (open blue circles) and qubit spectroscopy data (solid red circles) is indicated by black arrows on the detuning axis (see text for details). (**B**) Measured resonant vacuum Rabi mode–split cavity transmission spectrum T (blue line) versus probe frequency ν_{rf} at flux bias, indicated by blue arrows in (A). The solid red line is a fit to a double-peak Lorentzian. (**C**) Measured spectroscopic qubit line shape (blue line) versus spectroscopy frequency ν_s at flux bias, indicated by red arrows in (A). The solid red line is a fit to a Lorentzian.

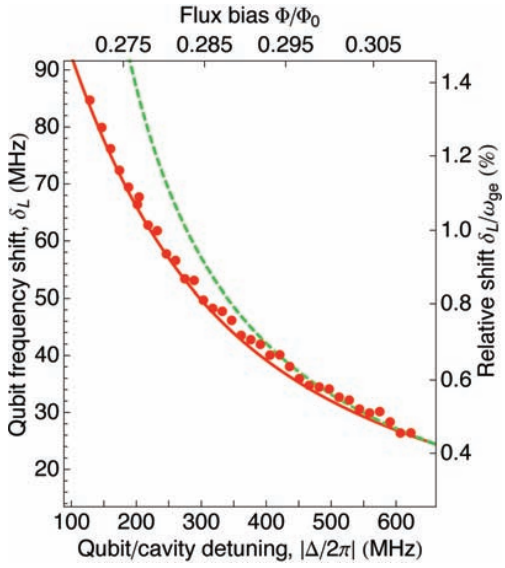

Fig. 3. Lamb shift. Difference between measured qubit-transition frequency $\tilde{\omega}_{ge}/2\pi$ dressed by the vacuum-field fluctuations (red circles) and calculated bare qubit-transition frequency $\omega_{ge}/2\pi$ versus qubit-cavity detuning $\Delta/2\pi$ (bottom axis) and normalized flux bias Φ/Φ_0 (top axis). The right axis shows the Lamb shift as a percentage relative to the bare qubit transition frequency. The red line is the predicted Lamb shift calculated with exact numerical diagonalization of the generalized Jaynes-Cummings Hamiltonian, and the dashed green line is g_{ge}^2/Δ from a dispersive approximation of Eq. 1.

We then determined the resonant qubit/field coupling strength g_{ge} by measuring the anticrossing of the flux-tunable qubit and the fixed-frequency resonator. The extracted frequencies $\nu_{1\pm}$ of the qubit/cavity superposition states $|n\pm\rangle$ for $n = 1$ photon are shown as blue circles in Fig. 2A as measured with a probe tone power populating the resonator field with much less than one photon on average. Here, the energies of the $|1\pm\rangle$ states were determined by measuring the photonic component of the joint qubit/field-state vector. On resonance ($\Delta = 0$), in which the joint states have equal qubit and photon character, we extracted the coupling strength $g_{ge}/2\pi = 133$ MHz from the observed vacuum Rabi-mode splitting (Fig. 2B), which in turn also allowed us to calculate the coupling between higher transmon levels and the cavity (*22*). The measured eigenfrequencies $\nu_{1\pm}$ were in excellent agreement with the exact numerical solution of the generalized Jaynes-Cummings Hamiltonian, taking into account higher qubit levels (Fig. 2A, solid green lines), at which we considered the qubit spectrum up to the fifth excited state and resonator states up to $|4\rangle$. At this point, we fully determined the parameters that govern the coupled qubit/resonator system and set out to spectroscopically measure the Lamb shift of the qubit because of the coupling to the fundamental mode of the resonator.

Using magnetic flux bias, we detuned the qubit to well below the cavity-resonance frequency ($|\Delta| >> g_{ge}$), at which the joint qubit/field state has a predominantly qubit character ($|e,0\rangle$) (Fig. 1C). We then spectroscopically determined the transition frequency $\tilde{\omega}_{ge}/2\pi$ between $|g,0\rangle$ and $|e,0\rangle$ by probing the resonator response in a dispersive quantum nondemolition measurement (*26*), which measures the qubit component of the joint state. At the largest investigated detuning ($|\Delta| \sim 620$ MHz), this state has a predominantly qubit character with ~99.5% probability for $|e,0\rangle$ and ~0.5% for $|g,1\rangle$ (*20*). In a typical qubit spectral line (Fig. 2C), the qubit line width is on the order of $\delta_{ge} \sim 3$ MHz, slightly power-broadened by the spectroscopy tone. Here it is important to point out that first we applied a long microwave pulse to the qubit to prepare a fully mixed state. Only after this, we applied a measurement tone to the resonator, the amplitude of which was used to readout the qubit state (*26*). In this pulsed spectroscopy scheme, excitation and measurement tones were separated in time, and the cavity was left approximately in the vacuum state $|0\rangle$, when the spectroscopy pulse was applied to the qubit. In contrast, performing a measurement with a continuous tone at the cavity frequency simultaneously with the spectroscopy pulse would result in an observation of a photon number-split qubit spectrum. In that case, the strong dispersive coupling leads to distinct, well-separated qubit lines that correspond to the individual photon number states, as is discussed theoretically in (*27*) and observed experimentally in (*28*).

We then sequentially reduced the detuning Δ and extracted the qubit transition frequency from the maximum in the pulsed spectroscopic line (Fig. 2C). The extracted dressed frequencies $\tilde{\omega}_{ge}/2\pi$ are shown as red circles in Fig. 2A. We observed that the measured frequencies coincide for all detunings with the frequencies of the $|1-\rangle$ state calculated from an exact numerical diagonalization of the generalized Jaynes-Cummings Hamiltonian accounting for the first five transmon levels. The difference between the measured and the bare qubit transition frequency (dashed slanted line), resulting from the interaction with the vacuum fluctuations, was clearly observed and well-resolved by many line widths. This represents a direct spectroscopic observation of the Lamb shift in a solid-state system and demonstrates the dispersive interaction of a superconducting qubit with the vaccuum field in a cavity.

We explicitly extracted the Lamb shift from the data versus flux-controlled detuning by subtracting the measured qubit transition frequency $\tilde{\omega}_{ge}/2\pi$ from the calculated bare frequency $\omega_{ge}/2\pi$, as shown by red circles in Fig. 3. For the measured range of detunings, we found that the Lamb shift varies from about 30 MHz at a detuning of $|\Delta|/2\pi \sim 620$ MHz to 85 MHz at $|\Delta|/2\pi \sim 130$ MHz, corresponding to a maximum value of roughly 1.4% of the bare qubit-transition frequency. The data are in good agreement with the Lamb shift that was calculated from the generalized Jaynes-Cummings Hamiltonian, including counter-rotating terms, shown as the solid red line in Fig. 3. For comparison, the Lamb shift g_{ge}^2/Δ expected from a simple dispersive approximation of Eq. 1 is shown as a dashed green line in the same plot. The dispersive approximation is in good agreement with the data for large Δ and is seen to break down for small Δ. The Bloch-Siegert shift (*29*) is small for the given coupling strengths in our sample and could not be resolved.

Over a range of detunings (Fig. 2A, black arrows), the energy of the coupled qubit/resonator system was extracted both from the photonic component, measured by probing the cavity resonance frequency, and the qubit component, measured spectroscopically. We observed virtually identical, and thus consistent, frequencies in the overlap region of the data from the two independent measurements (Fig. 2A, open blue and solid red circles).

Finally, we checked that the observed energy shifts were indeed solely due to the vacuum fluctuations of the radiation field and not confused with ac Stark shifts induced by residual photons in the cavity. To do so, we applied a continuous-wave coherent microwave field at the resonator frequency with the qubit in the ground state, populating the cavity with a small mean number of photons. We simultaneously used the same tone to perform a dispersive measurement of the qubit state. The resulting number-split qubit spectra (*27*, *28*) under weak qubit driving are shown in Fig. 4, B and C, for two different detunings (Fig. 4A, arrows). Each individual peak can be clearly associated with a photon number state

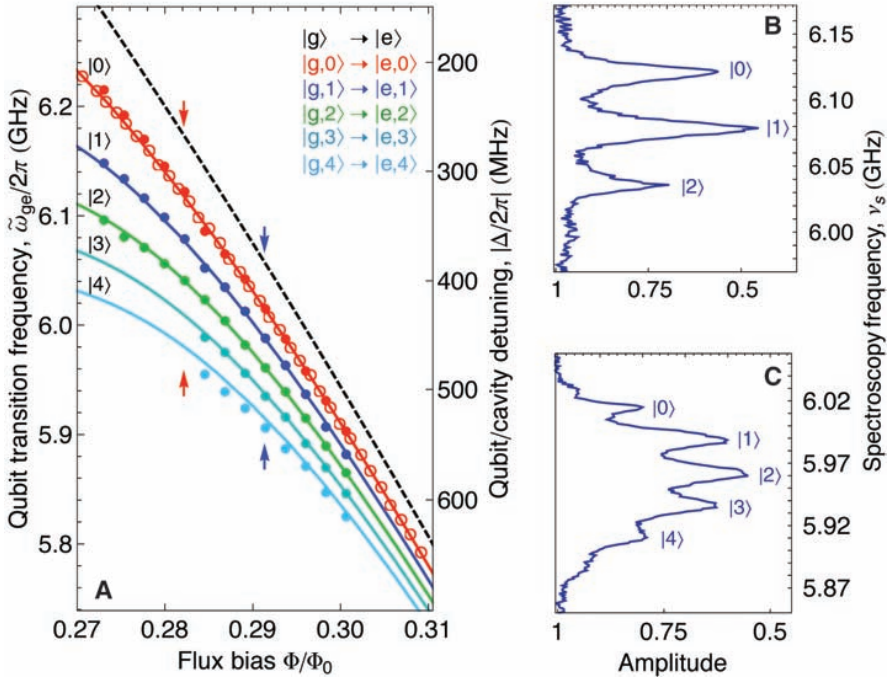

Fig. 4. Number splitting and ac Stark shift. (**A**) Spectroscopically measured qubit-transition frequency $\tilde{\omega}_{ge}/2\pi$ (data points) dressed by a weak coherent field. The solid circles with colors (red, dark blue, green, aquamarine, and light blue) correspond to number-split qubit transitions with $n = 0$, 1, 2, 3, and 4 photons, as indicated in the upper right-hand corner. Open circles are pulsed spectroscopy data from Fig. 2A. The solid lines are corresponding dressed-state energy levels calculated by exact diagonalization of the generalized Jaynes-Cummings Hamiltonian, and the dashed line is the bare qubit-transition frequency. (**B** and **C**) Measured number-split qubit spectrum at flux bias are indicated by blue and red arrows in (**A**). The photon number states $|n\rangle$ corresponding to each peak are indicated.

$|n\rangle$ of the cavity. The extracted peak frequencies for $n = 0$, 1, 2, 3, and 4 photons are plotted as solid circles in Fig. 4A. The corresponding transitions are also indicated by dotted arrows in Fig. 1C. Again, we clearly observed that the qubit frequency is Lamb-shifted with respect to its bare frequency by the vacuum state of the cavity. The pulsed spectroscopy data of Fig. 2A (open circles) are also in good agreement. Moreover, we resolved the quantum ac Stark-shifted qubit-transition frequencies of the corresponding photon number states $|n\rangle$ and their dependence on the flux-controlled detuning. As before, we were able to explain the observed frequencies of the individual transitions accurately, solving the generalized Jaynes-Cummings Hamiltonian numerically by taking into account up to five qubit (g, e, f, h, and i) and five cavity levels ($n = 0$, 1, 2, 3, and 4 photons) (Fig. 4A, solid lines). Only for $n = 4$ photons, small deviations between data and theory were observed. These are probably related to the limited accuracy with which the resonant frequency can be extracted from the number-split line, the width of which scales with $n\kappa$. This data consistently demonstrates that the measured frequency shift for an empty cavity ($n = 0$ photons) can be associated with the vacuum fluctuations of the cavity radiation field.

As a final check, we determined the background thermal photon number in our circuit QED system by probing the resonant vacuum Rabi-mode splitting. A small thermal population of the $|1\pm\rangle$ states can be detected through the transitions from the first doublet of the Jaynes-Cummings ladder into the second doublet $|1\pm\rangle \rightarrow |2\pm\rangle$, appearing as weak lines in the transmission spectrum of the resonator. The effective temperature of the radiation field was estimated to be $T_r \approx 90$ mK, corresponding to a mean thermal photon number of $\bar{n}_{th} \approx 0.03$, where we have analyzed in detail the amplitudes of these lines in the vacuum Rabi-mode splitting (*30*, *31*).

Another observation concerns the relative size of the Lamb and ac Stark shifts. In general for a two-level system, the ac Stark shift per photon is expected to be twice as large as the shift induced by the vacuum field. However, we made the surprising observation that the measured Stark shift per photon is in fact smaller than the Lamb shift (Fig. 4A). This phenomenon can be explained by considering the higher excited states of our qubit beyond $\{|e\rangle,|g\rangle\}$. As discussed theoretically in (*22*), the ac Stark shift per photon is renormalized by the presence of the third transmon level $|f\rangle$ and consequently reduced by a factor proportional to the level of anharmonicity. For the given measured anharmonicity of our artificial atom, we indeed reached the limit of $\delta_S/n < \delta_L$. In this way, the qubit appeared to couple more strongly to the vacuum field than to a single photon inside the cavity. Similarly, for two coupled strictly harmonic quantum oscillators, only a Lamb shift but no photon number–dependent Stark shift is expected, a situation that was approached in our experiments because of the limited anharmonicity of the qubit.

The Lamb shift induced in a solid-state quantum system by the vacuum fluctuations of the electromagnetic field in a resonator was observed spectroscopically. In resolving this effect, we explicitly demonstrate the presence of dispersive vacuum-field interactions in circuit QED and show that these can exceed the interaction with a photon-populated field. The clear observation of vacuum fluctuations in this strongly coupled system should serve as a motivation for further experiments aimed at investigating other effects triggered by quantum fluctuations of electromagnetic or even nanomechanical degrees of freedom in solid-state systems (*19*, *32*).

References and Notes

1. J. Schwinger, *Selected Papers on Quantum Electrodynamics* (Dover, New York, 1958).
2. P. W. Milonni, *The Quantum Vacuum: An Introduction to Quantum Electrodynamics* (Academic Press, New York, 1994).
3. H. Casimir, D. Polder, *Phys. Rev.* **73**, 360 (1948).
4. E. M. Purcell, *Phys. Rev.* **69**, 681 (1946).
5. W. E. Lamb, R. Retherford, *Phys. Rev.* **72**, 241 (1947).
6. H. Bethe, *Phys. Rev.* **72**, 339 (1947).
7. D. J. Heinzen, M. S. Feld, *Phys. Rev. Lett.* **59**, 2623 (1987).
8. M. Brune *et al.*, *Phys. Rev. Lett.* **72**, 3339 (1994).
9. M. Marrocco, M. Weidinger, R. T. Sang, H. Walther, *Phys. Rev. Lett.* **81**, 5784 (1998).
10. M. Niering *et al.*, *Phys. Rev. Lett.* **84**, 5496 (2000).
11. D. Walls, G. Milburn, *Quantum Optics* (Springer-Verlag, Berlin, 1994).
12. S. Haroche, J. Raimond, *Exploring the Quantum: Atoms, Cavities, and Photons* (Oxford Univ. Press, New York, 2006).
13. G. Khitrova, H. M. Gibbs, M. Kira, S. W. Koch, A. Scherer, *Nat. Phys.* **2**, 81 (2006).
14. R. J. Schoelkopf, S. M. Girvin, *Nature* **451**, 664 (2008).
15. J. Ye, H. J. Kimble, H. Katori, *Science* **320**, 1734 (2008).
16. A. A. Houck *et al.*, *Phys. Rev. Lett.* **101**, 080502 (2008).
17. J. Clarke, A. Braginsky, *The SQUID Handbook* (Wiley-VCH, Berlin, 2006).
18. M. A. Castellanos-Beltran, K. Irwin, G. Hilton, L. Vale, K. Lehnert, *Nat. Phys*. 10.1038/nphys1090 (2008).
19. C. Regal, J. Teufel, K. Lehnert, *Nat. Phys.* **4**, 555 (2008).
20. A. Blais, R. S. Huang, A. Wallraff, S. M. Girvin, R. J. Schoelkopf, *Phys. Rev. A* **69**, 062320 (2004).
21. A. Wallraff *et al.*, *Nature* **431**, 162 (2004).
22. J. Koch *et al.*, *Phys. Rev. A* **76**, 042319 (2007).
23. V. Bouchiat, D. Vion, P. Joyez, D. Esteve, M. H. Devoret, *Phys. Scr.* **T76**, 165 (1998).
24. J. M. Fink *et al.*, *Nature* **454**, 315 (2008).
25. J. Schreier *et al.*, *Phys. Rev. B* **77**, 180502 (2008).
26. D. I. Schuster *et al.*, *Phys. Rev. Lett.* **98**, 049902 (2007).
27. J. Gambetta *et al.*, *Phys. Rev. A* **74**, 042318 (2006).
28. D. I. Schuster *et al.*, *Nature* **445**, 515 (2007).
29. F. Bloch, A. Siegert, *Phys. Rev.* **57**, 522 (1940).
30. I. Rau, G. Johansson, A. Shnirman, *Phys. Rev. B* **70**, 054521 (2004).
31. L. Bishop *et al.*, *arXiv:0807.2882v1* (2008).
32. E. K. Irish, K. Schwab, *Phys. Rev. B* **68**, 155311 (2003).

33. We thank G. Blatter for stimulating discussions and L. Bishop, P. Studer, J. Koch, and R. Schoelkopf for their support in analyzing vacuum Rabi-mode spectra in the presence of thermal photons. This work was supported by the Swiss National Science Foundation and ETHZ. P.J.L. was supported by the European Commission with a Marie Curie Intra-European Fellowship. A.B. was supported by the Natural Sciences and Engineering Research Council of Canada, Canadian Institute for Advanced Research, and Fonds Québécois de la Recherche sur la Nature et les Technologies.

11 August 2008; accepted 20 October 2008
10.1126/science.1164482

A Cryptand-Encapsulated Germanium(II) Dication

Paul A. Rupar, Viktor N. Staroverov, Kim M. Baines*

Unlike cations of metals such as sodium or calcium, oxidized silicon and germanium centers generally require strongly bound covalent ligands. We report the synthesis and characterization of a germanium(II) dication in the form of the salt (Ge·cryptand[2.2.2])$(O_3SCF_3)_2$. The salt is isolated in 88% yield from the reaction of cryptand [2.2.2] and an N-heterocyclic carbene complex of $GeCl(O_3SCF_3)$ as an air-sensitive, white solid. The crystal structure of the salt shows minimal interaction between the cryptand-encapsulated germanium(II) ion and the two $^{-}O_3SCF_3$ counterions. These results suggest a widely expanded role of cryptands and related molecules in stabilizing nonmetallic cations.

For over a century, the periodic table has been an icon of science, providing a unifying vision for a seemingly diverse range of chemical facts. On the basis of their positions in the table, the main-group metals of groups 1 and 2 are expected to, and indeed form, stable free cations in solution with only weak coordination of the solvent. In contrast, elements in groups 13 to 15—particularly those of the first few periods: boron, silicon, phosphorus, and germanium—tend not to form cations, preferring to bond covalently to ligands. Despite the expectations, chemists have succeeded in synthesizing silylium (*1*, *2*) and germylium monocations with a vacant coordination site (*3*–*5*) in the condensed phase by employing two key strategies: (i) the use of bulky ligands and/or (ii) the use of noncoordinating counterions (*6*). Both tactics effectively stop the coordination of a fourth ligand to complete the octet at silicon or germanium (*7*, *8*). This methodology has been extended to silicon(II) and germanium(II) cations, which have only a single covalently bound ligand, as

Department of Chemistry, University of Western Ontario, London, Ontario, Canada N6A 5B7.

*To whom correspondence should be addressed. E-mail: kbaines2@uwo.ca